Computerized Medical Imaging and Graphics 78 (2019) 101664

Contents lists available at ScienceDirect

Computerized Medical Imaging and Graphics

journal homepage: www.elsevier.com/locate/compmedimag

Supporting diagnostics and therapy planning for percutaneous ablation of liver and abdominal tumors and pre-clinical evaluation

Dominik Spinczyk[a,*], Aleksandra Badura[a], Piotr Sperka[a], Marcin Stronczek[a], Bartłomiej Pyciński[b], Jan Juszczyk[b], Joanna Czajkowska[b], Marta Biesok[b], Marcin Rudzki[b], Wojciech Więcławek[b], Piotr Zarychta[b], Paweł Badura[b], Andre Woloshuk[b], Jarosław Żyłkowski[c], Grzegorz Rosiak[c], Dariusz Konecki[c], Krzysztof Milczarek[c], Olgierd Rowiński[c], Ewa Piętka[b]

[a] Evertop Sp. z o.o., 1-3 Długa, 41-506, Chorzów, Poland
[b] Silesian University of Technology, Faculty of Biomedical Engineering, 40 Roosevelta, 41-800, Zabrze, Poland
[c] II Department of Radiology, Medical University of Warsaw, 1a Banacha, 02-097, Warsow, Poland

A R T I C L E I N F O

Article history:
Received 29 January 2019
Received in revised form 21 August 2019
Accepted 3 October 2019

Keywords:
Computer aided liver ablation
Minimally invasive interventions
Image guided navigation

A B S T R A C T

Percutaneous ablation methods are used to treat primary and metastatic liver tumors. Image guided navigation support minimally invasive interventions of rigid anatomical structures. When working with the displacement and deformation of soft tissues during surgery, as in the abdomen, imaging navigation systems are in the preliminary implementation stage.

In this study a multi-stage approach has been developed to support percutaneous liver tumors ablation. It includes CT image acquisition protocol with the amplitude of respiratory motion that yields images subjected to a semi-automatic method able to deliver personalized abdominal model. Then, US probe and ablation needle calibration, as well as patient position adjustment method during the procedure for the preoperative anatomy model, have been combined. Finally, an advanced module for fusion of the preoperative CT with intraoperative US images was designed. These modules have been tested on a phantom and in the clinical environment.

The final average Spatial calibration error was 1,7 mm, the average error of matching the position of the markers was about 2 mm during the entire breathing cycle, and average markers fusion error 495 mm. The obtained results indicate the possibility of using the developed method of navigation in clinical practice.

1. Introduction

Percutaneous ablation methods are used to treat primary and metastatic tumors. Of the various procedures, the use of thermal ablation in the liver is perhaps best mastered and understood. Due to the effectiveness of the method proven by numerous scientific studies, thermal ablation has been included in the official/main treatment regimens of hepatic neoplastic changes, e.g. by the Barcelona Clinic Liver Cancer (BCLC) or European Society of Medical Oncology (ESMO). Due to its sub-diaphragmatic position, the liver exhibits significant motility during respiration that is stronger than other parenchymal abdominal organs, which is important when planning and performing the procedure. Ablative procedures are usually performed under general or intravenous anesthesia, with percutaneous access aseptic properties. Various imaging methods are used to monitor ablative procedures, the most widely used are ultrasonography (US) and computed tomography (CT). Monitoring the procedure under the control of CT and possibly CT fluoroscopy guidance allows the surgeon to determine the position of the tool (needle, electrode, antenna) with respect to the borders of the organ being treated, as well as to structures as the intestines, lungs or large vessels. Due to the limited tissue resolution of CT in the phase without contrast administration, correct positioning of the tumor ablation tool requires two-way combination of two imaging techniques (CT and US) or image fusion without contrast enhancement with the images of the organ in the contrast enhancement CT (Pereira, 2007; Crocetti et al., 2010).

The problem of monitoring the ablation tool position in CT can be solved partially by implantation of fiducial markers in the tumor area before the procedure, as is the case before radiotherapy plan-

* Corresponding author.
E-mail address: dspinczyk@polsl.pl (D. Spinczyk).

https://doi.org/10.1016/j.compmedimag.2019.101664
0895-6111/

ning. However, this approach is rarely used - it would optimally require the implantation of several markers defining the tumor boundaries, and the introduction of each marker corresponds to an invasive procedure similar to that of the core needle biopsy. The need for systems supporting the ablation planning and performing procedures increases when the relation of the tumor to the vessels is critical to success - this is dictated by safety (e.g. hemorrhagic complications) as well as the effectiveness of the procedure (due to the known effect of heat loss in the vicinity of large vessels in the thermoablation technique). The ideal support system should offer a reliable fusion of images, including the organ's respiratory motion during the procedure (Puijk et al., 2018).

The continuing development and adoption of image navigation systems is part of the trend towards precise and minimally invasive procedures, which result in less trauma and faster patient recovery (Peters and Cleary, 2008). Imaging systems are widely used in procedures in which the reference points are rigid elements of the skeleton (treatment of the brain and spinal cord). However, when working with the displacement and deformation of soft tissues during surgery, as in the abdomen, imaging navigation systems are in the preliminary implementation stage. Phee and Yang (Phee and Yang, 2010) present the possibility of using magnetic resonance (MR) and CT pre-operative images and their fusions with intraoperative US images. However, they pay attention to the initial state of systems' advancement due to the difficulty in modeling the deformation of organs during the procedure. Neshat et al. (Neshat et al., 2013) present an approach to liver navigation by creating an image of a three-dimensional operating field based on a 2D US image sequence. The study from Kenngott et al. (Kenngott et al., 2014) evaluated the feasibility of a commercially available augmented reality (AR) guidance system employing intraoperative robotic C-arm cone-beam computed tomography (CBCT) for laparoscopic liver surgery. In the phantom experiment, the AR system shows a mean target registration error of 0.96 ± 0.52 mm, with a maximum error of 2.49 mm. Spinczyk (Spinczyk, 2015) proposed the approach to determine spatio-temporal correspondence between the US sequence and the 4D computed tomography (CT) examination. It was developed, implemented and tested qualitatively in 10 clinical cases and received qualitatively satisfactory results (visual assessment of mergers by radiologists), which were not quantitatively evaluated.

The typical navigation system supports the user at the diagnosis, planning, and therapy stages. At all of these stages, the patient's anatomical model is crucial for the success of the navigation system. At the diagnostic stage, it can better differentiate the pathological change. At the planning stage, it allows the surgeon to plan the trajectory of the tool and bypass anatomical structures. At the therapy stage, it helps to minimize the invasiveness of intervention.

The aim of the current study is to propose the overall methodology which supports the diagnostics and therapy planning for percutaneous ablation of liver tumors with pre-clinical evaluation. It includes preoperative phases with patient – related model design, respiratory-related amplitude measure, calibration and therapy planning. Patient and model registration as well as preoperative CT and intraoperative US image fusion with intersurgical image navigation in real time permits the system to be employed as an additional set-up during the ablation procedure. The main contribution brought by the paper can be identified in designing a general workflow of a system for a computer-aided diagnosis and therapy in a complex medical procedure of ablation. The entire project involved several groups of experts: medical doctors, biomedical engineers, software developers. The system is targeted at the entire process, not only individual tasks and procedures, like image segmentation or computer-aided therapy planning. Nonetheless, each of seven steps stands for a vital contribution into the system: data acquisition with marking protocol, patient-related model design in terms of dedicated step-by-step segmentation algorithms, respiratory-related measurements, calibration protocol, therapy planning, patient registration in clinical conditions, and intraoperative US—CT fusion in real time. According to the authors' knowledge, no such system exists in an analogous form. In order to validate the system we performed quantitative and qualitative evaluation of its components, all reported in Section 3.

The paper is organized as follows: the Material and Methods section presents the overall methodology and discusses each phase. Section 3 shows the evaluation results at various phases of the workflow. The results obtained and conclusions are analyzed in the Discussion section.

2. Material and methods

The overall computer assisted minimally invasive system contains several steps. Most of them are preoperative phases, but the last two are performed during the surgery. The aim of the preoperative steps is to collect and process the multimodal image data, extract the required features, calibrate the surgical tools, and develop the therapy-planning module. The intraoperative steps perform the system components registration and multimodal image data fusion. Thus, the preoperative steps include:

1 Acquire data during inhalation and exhalation a 4D image space. Markers are fastened on the patient's skin in order to allow further calibration.
2 Design a patient – related model with accurately labeled selected anatomical structures and the target lesion to be ablated.
3 Determine the respiratory-related amplitude by measuring the shift of the lesion center of gravity during respiration.
4 Calibrate the US probe and biopsy needle.
5 Plan the therapy by selecting the percutaneous entry point and the optimal pathway to the target without violating vital anatomical structures. Intersurgical steps contain:
6 Locate the patient and their model registration by applying the algorithm for rigid adjustment of the image coordinate system to the patient's physical coordinate system.
7 Fuse the preoperative CT and intraoperative US image and the real-time image navigation during surgery.

2.1. Preoperative patient data acquisition

In order to describe the respiratory cycle of internal organs it is necessary to provide appropriate image data presenting their extreme positions, i.e. on the inhale and exhale. For this purpose, the CT acquisition protocol is adjusted. The differences are as follows: two scans are performed in the early and late venous phase - on inhalation and exhalation, respectively. The examination is carried out with 5–7 markers on the patient's body. Hypoallergenic markers have received a certificate of compatibility with CT systems and do not reduce image quality. In order to assure the repeatability of the respiratory motion, the image acquisition is performed after the patient is anesthetized and intubated.

2.2. Patient-related model

The 3D model is based on stable and accurately located anatomical structures, which are detected automatically (Fig. 1) in the CT study. Bony structures are natural candidates. Then, the abdominal cavity is delineated. Selected points automatically marked on the spine serve as reference points and the abdominal cavity edge restricts the segmentation area. Given the starting points, segmentation modules are described. Due to organ variability, anatomy-specific modules have been defined.

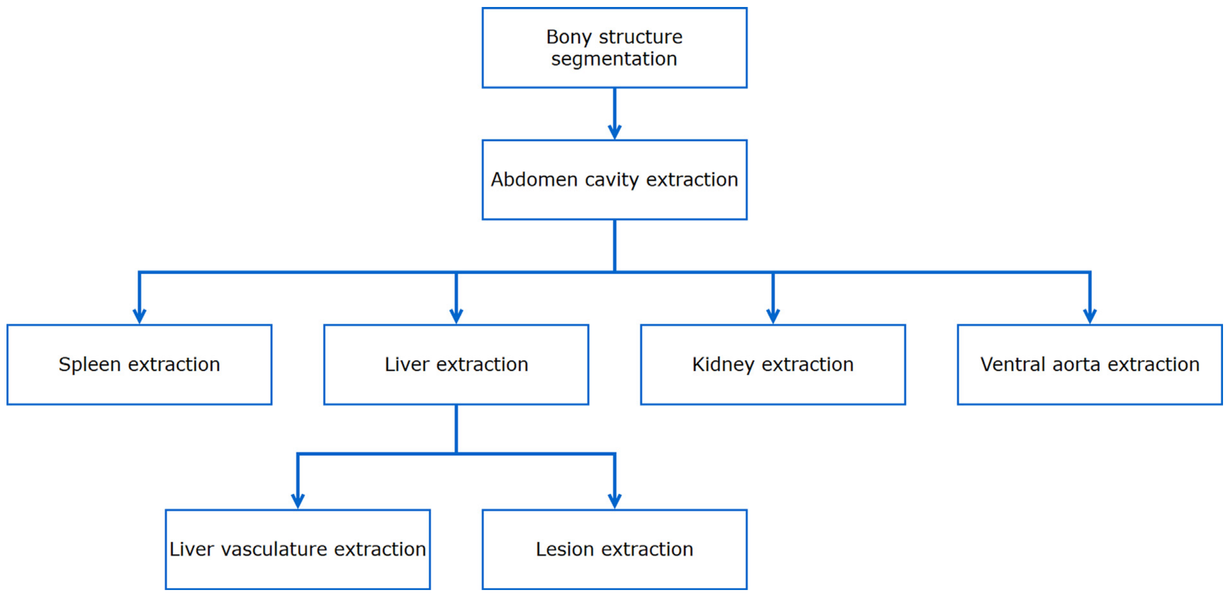

Fig. 1. Workflow of the patient specific anatomical model design.

2.2.1. Bone structure and abdominal cavity segmentation

The skeleton contains several characteristic landmark points, which give reference coordinates to facilitate segmentation of abdominal organs. The first stage of the method is discarding the upper one third of the volume. As a result, the ends of the ribs are removed from the region of interest (ROI). Then, the image is binarized at 160 Hounsfield units (HU). The remaining structures are bone tissues, few soft tissues, contrast agent inside the bowels, and the board from the CT device under the patient. After separating and labeling consistent areas, the largest one is kept and the others are removed. The remaining voxels belong to the spine and the pelvis. These structures are usually not perfectly perpendicular to the scanner's long axis, due to position of the patient or their eventual scoliosis. Normalization of orientation is required. This is performed by finding the extreme points of iliac wings and ischial bones. With these points, rotations in frontal and axial planes normalize the orientation of the image.

The landmarks defining the area of the abdominal cavity for further steps of the workflow are the sacral promontory, anterior superior iliac spines, superior point of pubic symphysis, and xiphoid process. All the points, except the last, are located on the pelvis. To find the pubic symphysis automatically, the CT slices are checked in sequence from bottom until two pubic bones disconnect. The anterior superior iliac spines are the points which maximally project anteriorly on the segment between the pubic symphysis and promontory. The xiphoid process is located in the first slice where two costal margins of the chest connect.

Abdominal cavity segmentation delineates the ROI that is subjected to further processing.

The abdominal cavity segmentation over the ROI consists of a series of operations. First, the patient body is delineated on considered slices. Next, procedures for segmentation and removal of four tissues takes place: fat, bones, lungs, and muscle tissue. Each procedure employs dedicated binarization and morphological corrections. The remaining regions are subjected to segmentation leak detection in the vertebrae area with the shape-based lower abdominal cavity boundary reconstruction.

2.2.2. Spleen and liver (parenchymal organs) segmentation

The spleen and liver segmentation starts with an automatic seed point selection procedure. For each structure one seed point is required. Its selection procedure is based on the location and shape normalization for bringing them into a common coordinate system with an internal organs probability map. The center of gravity of an organ probability map is a selected seed point (Juszczyk et al., 2015). The seed point stands for a center of the ROI at a default size. It allows the texture pattern and statistical intensity-based parameter (mean intensity μ and standard deviation of mean intensity σ_μ) to be determined. Then, the image is thresholded with adaptively defined thresholds employing the experimentally adjusted coefficient α within the range of $\mu \pm \alpha \cdot \sigma_\mu$. Next, two filtering procedures are carried out simultaneously: the texture filtration with a structuring element found within the ROI and the entropy filtration (Gonzalez et al., 2004), both of equal mask size. The texture filtration enhances the regions with similar texture patterns. However, due to the similar textures of the liver and spleen, over-segmentation appears quite often. Thus, an edge enhancement entropy filter is implemented (Fig. 2). Finally, both images, texture filtered I_{TF} and entropy filtered I_{EF}, are both normalized linearly into the [0, 1] range and combined:

$$I_{out} = norm(I_{TF}) \cdot (1 - norm(I_{EF}))$$

Labeling yields the final image.

2.2.3. Kidney segmentation

The fully-automatic kidney segmentation algorithm consists of several steps. The workflow employs the skeleton detection (Fig. 3), which detects a first-level ROI. The next stage is a second-level ROI detection. There are two, symmetrically oriented windows (a symmetry with respect to the spine) containing the left and the right kidney. Both regions (the first- and the second-level) create the final ROI, which is a starting point for the next kidney segmentation procedure (Wieclawek, 2018). Kidney seed points are searched for during further processing. The search starts from properly oriented diagonals of cuboids (main diagonal and anti-diagonal), imposed on the soft tissues subset (black diagonals of rectangle windows in Fig. 3). Detection of kidney seeds consists of a multi-stage morphological image reconstruction. Adaptive filtering using anisotropic diffusion and morphological corrections are used at this stage. As a result, a single spatial structure remains in the image. It is subjected to the active contour algorithm that demarcates the kidney edges (Chan and Vese, 2001).

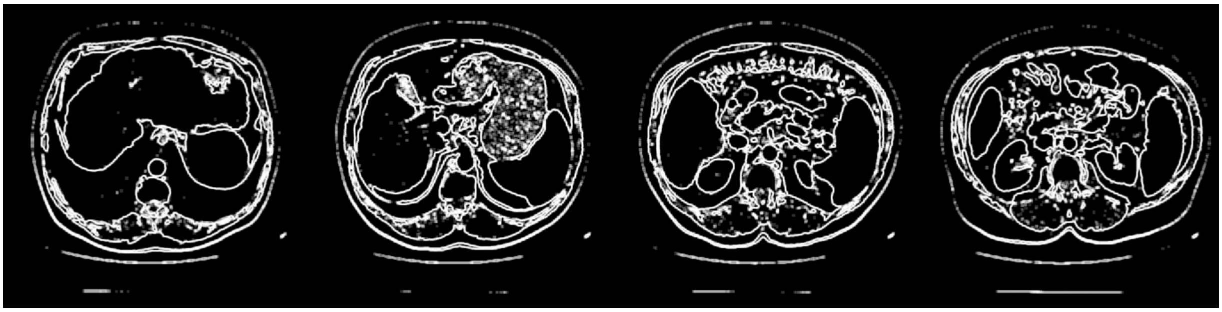

Fig. 2. Illustration of the entropy filtration results.

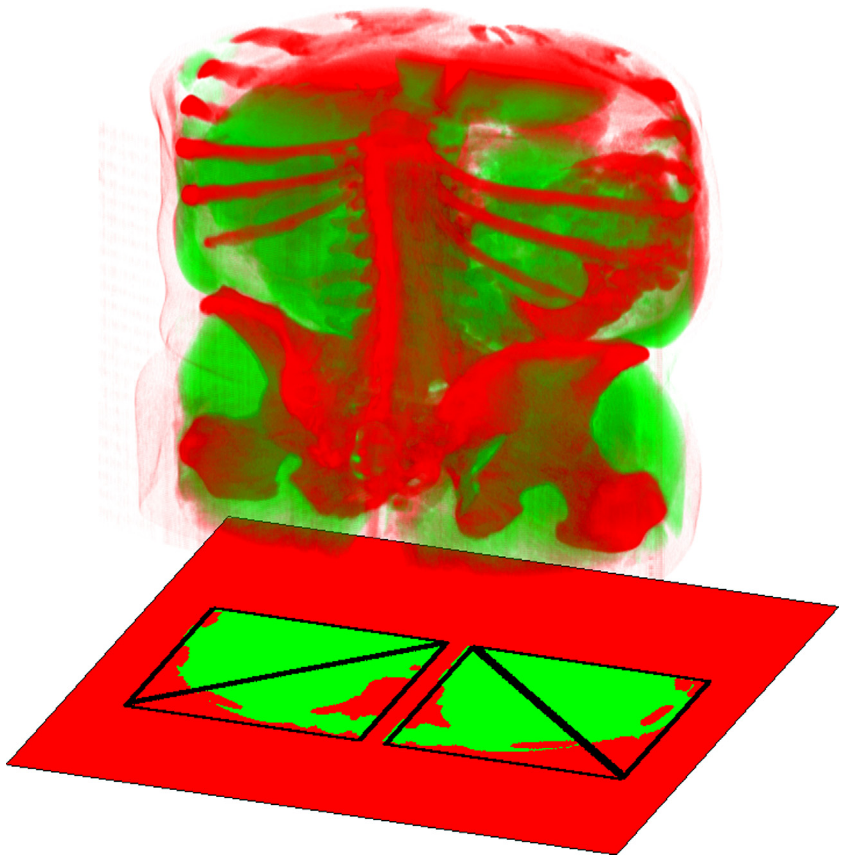

Fig. 3. Multi-level ROI (red voxels - irrelevant areas and patient skeleton, green voxels - important regions i.e. soft tissues, black lines - ROI). (For interpretation of the references to colour in this figure legend, the reader is referred to the web version of this article).

2.2.4. Aorta segmentation

The abdominal aorta segmentation step begins with a starting point selection procedure. The ROI in the CT slices is limited by previously identified bones and starts from a beginning of the tenth rib. The analysis ends at the beginning of the bifurcation of the aorta. The Fuzzy C-Means (FCM) clustering procedure is applied to the first analyzed image. The bright object above the spine is considered as the sought aorta and its midpoint of gravity indicates the starting point for further analysis. The ROI is defined as the square region of the size of 8 cm with the center located in the starting point. The Canny edge detector algorithm (Canny, 1986) is applied to the already defined ROI. The extracted edges indicate the segmented aorta region. Due to the edge discontinuity, the active contour model proposed by Kass et al. (1988) is introduced. The external contour energy is defined on the basis of gradient image on previously obtained edges, whereas the internal one defines physical features of deformed curve presenting its circular shape. Moreover, the set balloon force F prevents the curve from shrinking (Cohen and Cohen, 1993). Since the classical active contour approach is limited by a local character of the estimated gradient and will not cause movement of the curve placed far from the edges, the Gradient Vector Flow (GVF) (Chenyang Xu and Prince, 2019) technique is used. The center of gravity of the segmented object is projected to the subsequent slice as the starting point for its analysis. In order to reduce the number of imperfect segmentations on single slices, a post processing analysis is applied. The statistically important changes in the aortic area are then detected and an interpolation step is performed.

2.2.5. Liver vasculature segmentation

The analysis is performed on the contrast enhanced CT study with an already delineated liver. From the input mask M_L, two auxiliary masks are formed: an inner mask M_{LI} and an outer mask M_{LO}. The inner liver mask M_{LI} defines the internal liver tissue where vasculature segmentation starts. It is created by moving the M_L mask border inwards by a specified distance. the outer mask M_{LO}, created as a convex hull of the original liver mask M_L, defines a region where the vasculature segmentation is to be continued. This way, the liver vasculature below the visceral liver surface can be segmented. The input image is intensity windowed to the confidence interval around medial intensity based on intensity statistics within the inner mask M_{LI} region.

Vasculature detection utilizes Frangi's vessleness filter employing hessian eigenvalue decomposition (Frangi et al., 1998). The detection is performed for several scales of analysis (corresponding to the radii of the blood vessels) on input image region defined by outer mask M_{LO}. The maximum response over the scales is calculated forming image I_F that defines a weight for contrast enhancement performed on the image. This is performed by intensity increment with saturation. Next, the image is Gaussian-smoothed and subject to the segmentation stage. The segmentation, employing the region growing approach with intensity criteria, starts from a percentage of voxels having the highest vesselness response within the inner mask M_{LI}. To prevent segmentation leaks, forbidden regions are defined by areas of low vesselness response value within the region M_{LO}. Finally, the result is subjected to morphological closing. Upon user interaction starting points may be defined apart from those found in an automated manner. Control parameters of the algorithm are also user alterable.

The method does not make use of the information about the image acquisition phase (arterial, hepatic/portal, venous) it segments the vasculature having higher intensities (contrast enhanced CT acquisition protocol) than the surrounding tissues. By default it is performed for scales between 2.0 mm and 10.0 mm which correspond to the diameters of the vessels being searched for. Exemplary segmentation results is shown in Fig. 4. However, the image voxel size limits the possibility of accurate hessian determination in 3D, especially when the image resolution in z-axis is more than 3 times lower than in the x–y (axial) plane. Moreover, the used segmentation approach as well as the post-processing step (morphology) requires the segmented structure to be fully connected. Thus, it can be stated that the algorithm can detect and segment vessels which cross-section is at least 3×3 pixels. The corresponding diameters in mm stem from the image spatial resolution.

2.2.6. Lesions segmentation

The focal lesion segmentation relies on two seed points indicating central points of the lesion on its external slices (s1 and s2 in Fig. 5a). It is possible to involve more than two seeds, each located in a single slice between the external slices (s3 in Fig. 5a). Either way, the closest pairs of seed points are connected in order to determine the nodule axis, defining central points on each slice under consideration. The central points stand for the centers of circles – initial contours for the active contour segmentation. The radius of each circle depends on the slice location: smaller near to the external slices and larger in the central part (Fig. 5a). The radii depend also on the estimated nodule size, D_z, based on the distance between external points. D_z affects also the size of the volume of interest (VOI), which is extracted around the nodule axis before further processing. First, the VOI is subjected to a three-dimensional anisotropic diffusion filtering adjusted to lesion objects characteristics (Perona and Malik, 1990; Badura et al., 2016). Then, the Chan-Vese active contour segmentation is employed (Chan and Vese, 2001). The number of contour evolution iterations is set adaptively based on both Dz and slice position within the VOI. Finally, the obtained object is processed by means of morphological closing (Fig. 5b).

2.3. Respiratory-related breathing amplitude measurement

In the tracking and gating methods, a signal representing the phase of the respiratory movement is necessary. There are various ways of observing this movement in the literature. One of the possible ways is to follow the breath by observing the chest movement. Breath is a variable process over time, so there is a need to average it (McClelland et al., 2006; von Siebenthal et al., 2007). Usually, the amplitude of the respiratory movement is not directly assessed. Only the so-called phase of respiratory movement is indicated. The filtration of the signal obtained from markers, subjected to the Gaussian filtering, unambiguously determines the minima at times t_i^{min} and maxima at times t_i^{max}, $i = 1, \ldots, N^{max}$ that refer to as the average of the zero and maximum phase of the respiratory cycle, respectively. The maxima are assigned the average phase over all maxima, $\underset{-}{\varnothing}^{max}$, which is calculated according to the formula (Rijkhorst et al., 2010):

$$\underset{-}{\varnothing}^{max} = \frac{1}{N^{max}} \sum\nolimits_{i=1}^{N^{max}} \frac{t_i^{max} - t_i^{min}}{t_{i+1}^{min} - t_i^{min}}$$

The breathing phase $\varnothing_j$ displayed in time j is interpolated linearly (Rijkhorst et al., 2010):

$$\varnothing_j = \{ \left(\frac{t_j - t_i^{min}}{t_i^{max} - t_i^{min}} \right) \underset{-}{\varnothing}^{max} \text{ ; } for\ t_i^{min} \le t_j < t_i^{max}\, \underset{-}{\varnothing}^{max} + \left(\frac{t_j - t_i^{max}}{t_{i+1}^{min} - t_i^{max}} \right) \left(1 - \underset{-}{\varnothing}^{max} \right) \text{ ; } for\ t_i^{max} \le t_j < t_{i+1}^{min}$$

The shift of the already extracted centers of gravity of the lesion at inspiration/exhalation, determine the respiratory amplitude of the lesion. The input data for breathing amplitude measurement are 3D CT scans limited to the extreme positions of the inhalation and exhalation. The amplitude of the respiratory movement of focal lesions is shown in Fig. 6.

2.4. System calibration

Calibration of the ultrasound probe consists of finding an appropriate transformation between individual coordinate systems and time calibration. The purpose of the calibration is to present in a single coordinate system: a model of preoperative anatomy of the patient, the patient located on the operating table, ablation needle, and the ultrasound image.

The calibration process includes both spatial and time calibration. Spatial calibration is referred to as a transformation between the object coordinates and markers that are rigidly connected to the object (patient, phantom). It is performed in two phases. First, a pivot calibration calculates the offset between the stylus tip/stylus and the attached marker. Attaching the tip to a stationary point and tracking the motion of sensor positions yields the position of the indicator tip in coordinate system. Spot registration is used to calculate the transformation between the object and the marker. Secondly, the multi-layer calibration determines US image location. It is based on the analysis of the trajectory of markers attached of the US probe (Lasso et al., 2014).

In contrast, the time calibration, based on the PLUS (Public Software Library for UltraSound) library, assumes that data sources are acquired with an unknown but constant time shift. This method consists of a single 10-second trace followed by the imaging trace performed while moving the transducer along a continuous quasi-periodic trajectory pattern (e.g., moving the camera up and down) (Lasso et al., 2014).

At this stage the system is ready for therapy planning.

2.5. Therapy planning

Therapy planning requires a selection of an optimal path from a percutaneous access point to the target lesion subjected to ablation and omitting all vital anatomical structures. The search is based

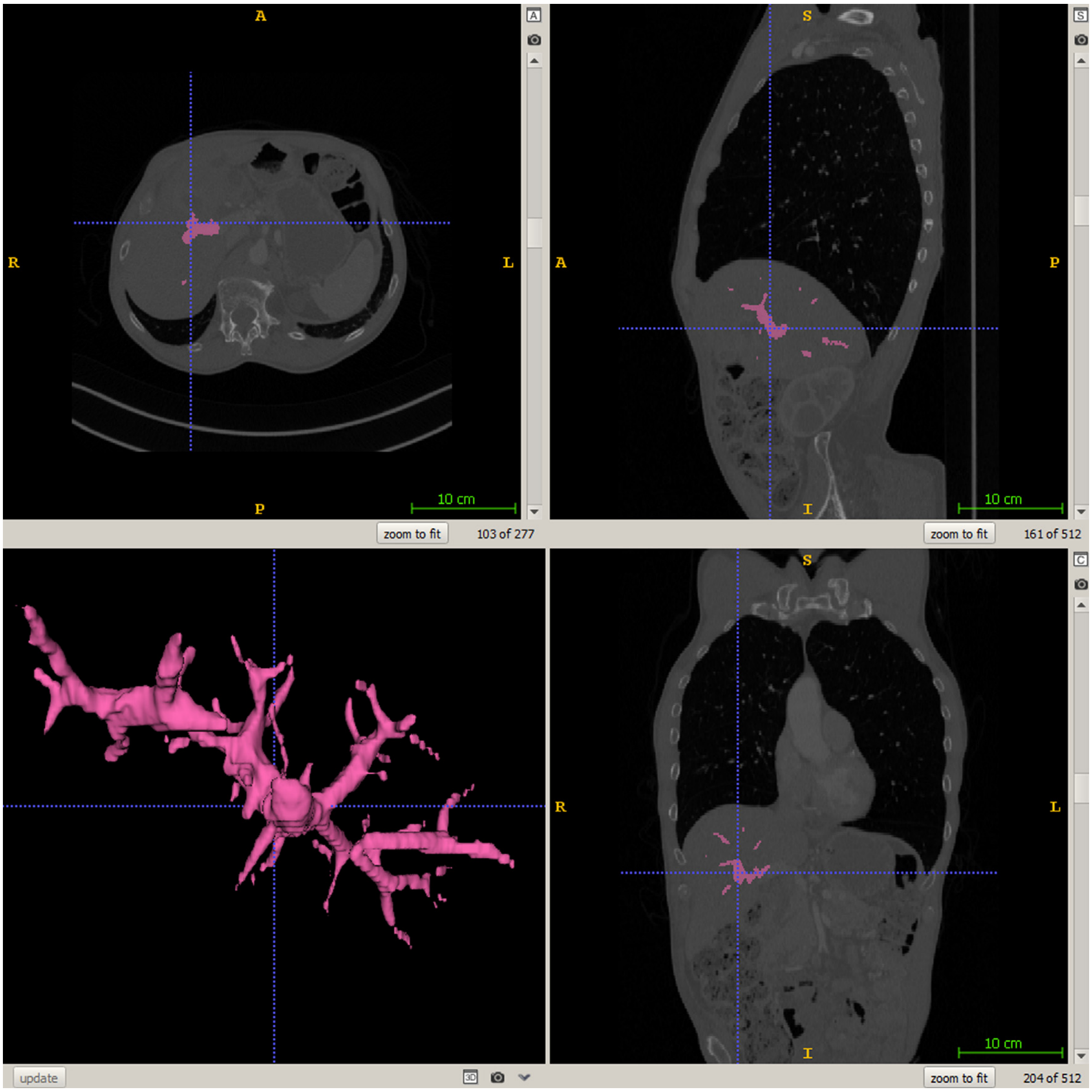

Fig. 4. Illustration of the liver vasculature segmentation results. A 3D view shown (bottom left) along with selected projections.

on an analysis of the CT scan (additionally US may be employed) and the patient-related model of anatomical structures determined according to Section 2.2. The choice of the entry point and the path itself corresponds to the respiratory motion of the abdominal organs. Example of segmentation results and selected entry and target points are shown in Fig. 7.

2.6. Pre-surgical patient registration

Patient registration requires the preoperative CT data to be processed and displayed on a surgical monitor as a 3D patient-related model. Data acquisition in the inhale and exhale phases are subjected to further processing. Automatically selected starting points of selected anatomical structures are followed by anatomy-depended segmentation procedures (Section 2.2).

A reference between the preoperative patient model and the patient will enable the model to be used during the procedure. The matching process requires a spatial alignment or its estimation for two sets of images or points. Due to misplacement and/or possible changes in shape of various anatomical structures, implementation of a rigid algorithm yields only unambiguous mapping of surface points to the model points and thus it is employed only at a very early stage of the patient registration.

Due to the existing analytical form of the solution, which is used to calculate a rigid transformation between two coordinate systems, in this study the algorithm by B. K. Horn (Horn et al., 1988) was used to perform a rigid adjustment of the image coordinate system and patient physical coordinate system. The rigid transformation consists of a translation - shifts in X, Y, Z and rotation (angles are expressed in quaternions). This algorithm calculates the transformations between both coordinate systems referred to as a coordinate system of the image navigation system. The sets of corresponding points are called the source and target sets, respectively. The adjustment is based on minimizing the error of the mean square root of the parameters of the resulting transform, i.e. the distance between the corresponding points of the target set R (reference) and the transformed points of the source set T (template). Parameters of rotation and translation matrix are found by the decomposition matrix of the source and target set points correlation (Peters and Cleary, 2008).

2.7. Intraoperative US images and CT model real-time fusion

After performing successfully previous steps, the fusion of a preoperative CT image and intraoperative US image can be performed. This means that both types of images are displayed in

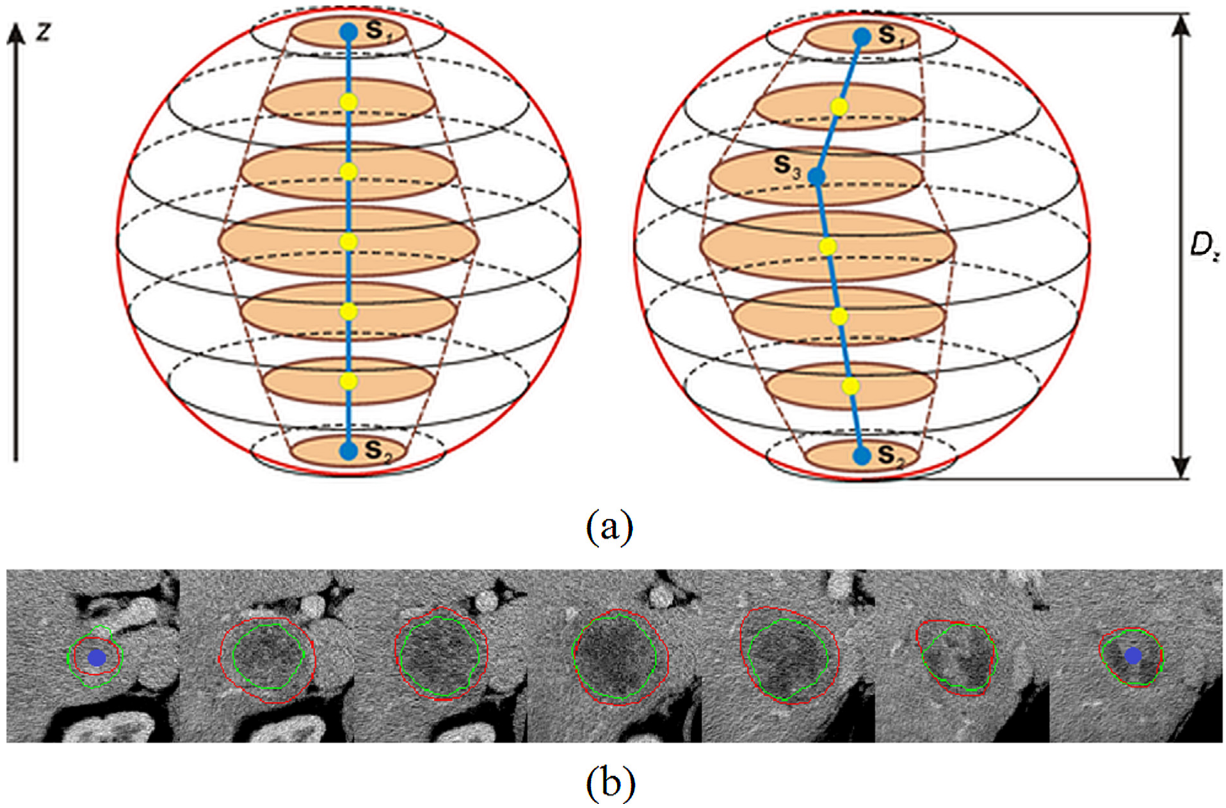

Fig. 5. Illustration of the nodule axis and initial contours (a) and a slice-by-slice visualization of an exemplary lesion delineated by the method (green contour) and the expert (red contour) along with the seed points indicated on the first and last slice (blue dots) (b). (For interpretation of the references to colour in this figure legend, the reader is referred to the web version of this article).

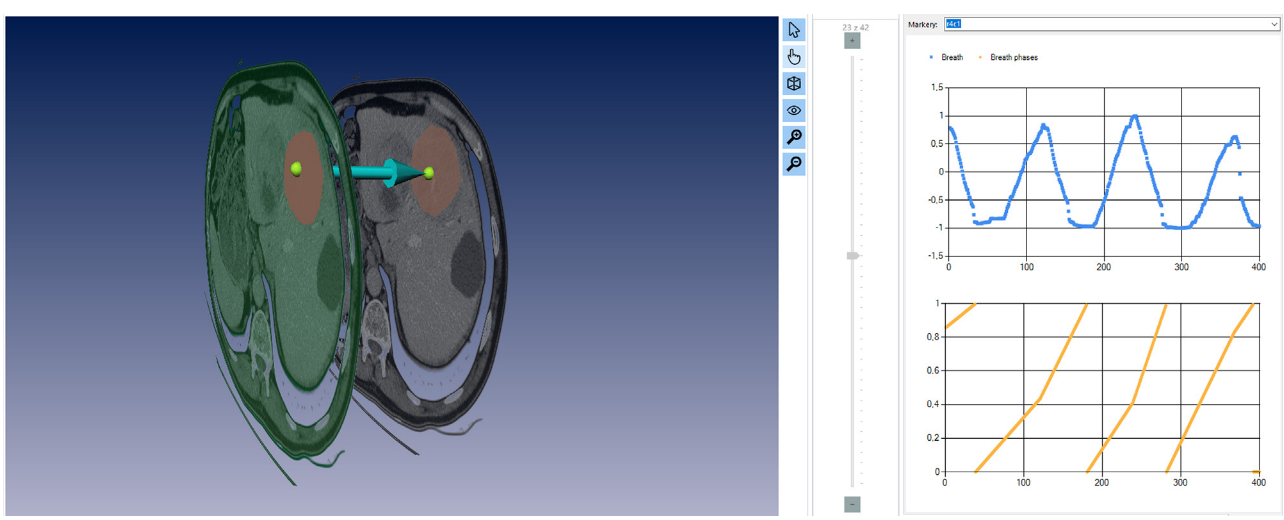

Fig. 6. Center of gravity points and breathing amplitude (inspiratory-exhale) for a liver lesion.

one coordinate system. The real time performance including the spatio-temporal calibration allows the procedure to be intraoperative.

The image fusion makes apparent structures invisible in US images. In the designed application, it is presented in the form of a three-dimensional scene (Fig. 8 - left) superimposed over the corresponding CT section (Fig. 8 - right). The figure shows the fusion of the calibration phantom US image as “interlaced strands” whose cuts in the fusion image are marked with color (top of the drawing). The lower part of the figure shows the liver in a fused US-CT image during ablation.

3. Results

Evaluation process of the proposed system is divided into independent parts. In step 1, (Data acquisition) a designed data acquisition protocol was employed. Evaluation of stages 2, 3 and 5 (Segmentation and Determination the respiratory phase, Therapy planning) was performed by means of 20 clinical studies of patients with liver cancer and is presented in Section 3.1. Steps 4, 6 and 7 (System calibration, Patient registration and Fusion of the image) are evaluated using a calibration phantom as presented in Section 3.2. and 3.3.

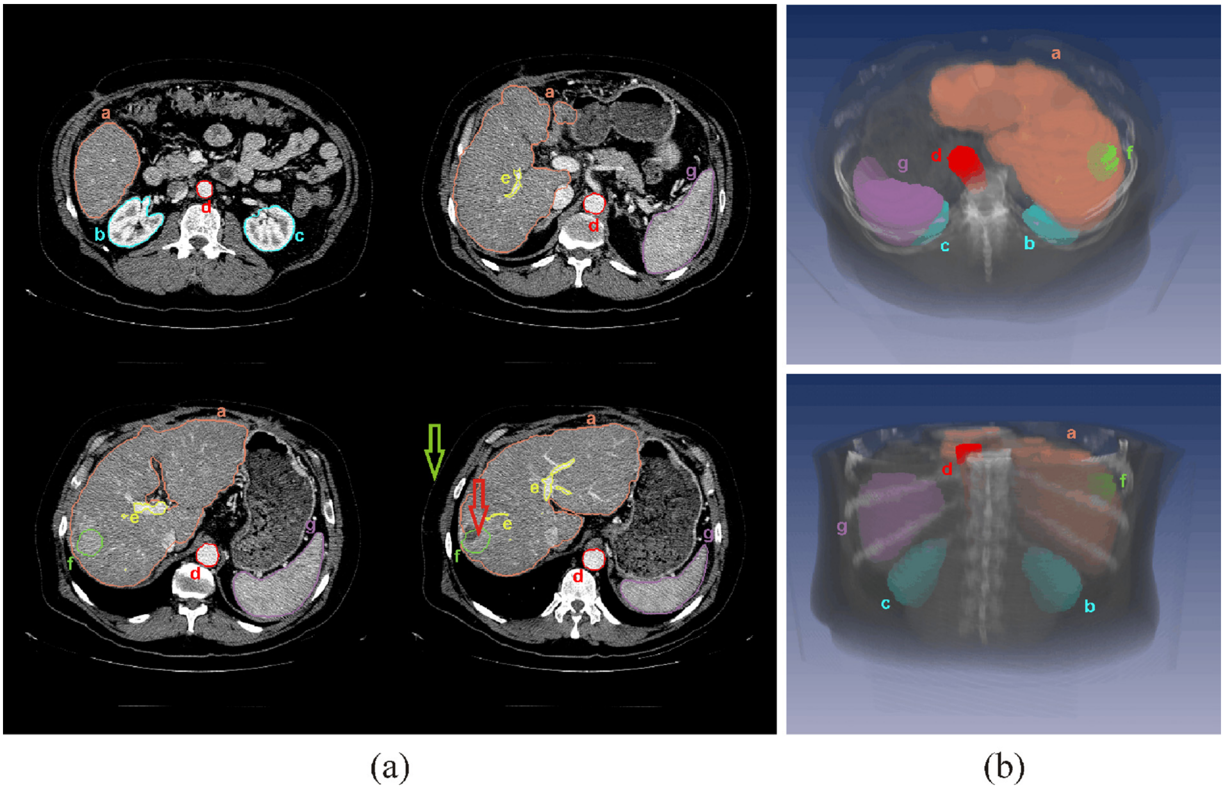

Fig. 7. An example of a patient anatomy model and selection of entry (green arrow) and target points (red arrow): four axial slices (a) and two 3D views (b). Notation of structures: a - liver, b - right kidney, c - left kidney, d - abdominal aorta, e - hepatic vein, f - focal lesion, g - spleen. (For interpretation of the references to colour in this figure legend, the reader is referred to the web version of this article).

3.1. Image analysis evaluation

Accuracy of the image analysis including segmentation as well as image fusion influences the overall system performance. The developed segmentation algorithms were verified on 20 CT scans of abdomen studies with contrast enhancement. The evaluation is based on the DICE coefficient - a coefficient of similarity and the degree of image overlap:

$$DICE\left(I_{Ref}, I_{Seg}\right) = \frac{2\left|I_{Ref} \cap I_{Seg}\right|}{\left|I_{Ref}\right| + \left|I_{Seg}\right|} \cdot 100\%$$

where I_{Ref}, I_{Seg} denote the reference contour pattern of the segmented object and the contour obtained by the segmentation algorithm, respectively, both being 3D volumes. The ground truth delineation was prepared by an expert on each slice.

3.2. System calibration and patient position registration assessment

The Fiducial registration Error (FRE) measure is employed to evaluate the calibration and patient position registration. It is defined as:

$$FRE^2 = \frac{1}{N}\sum\nolimits_{i=1}^{N}\left|Rx_i + t - y_i\right|^2$$

where N is a number of markers, x_i and y_i are the i-th marker positions in the first and second coordinate system, respectively. R and t are the rotation and translation matrices, respectively.

In both cases, the position of fiducial points in one coordinate system is converted to the second coordinate system using the transformation found in the calibration process. In a rigid adjustment of the patient position, the tracer markers indicated by the radiologist in CT images and obtained from the position tracking system in the patient system are subjected to analysis. In the ultrasound head calibration, the known actual position of the selected elements of the calibration phantom of known geometry and the positions of these elements visible in US images are processed. The results are shown in Table 2 and 3.

3.3. Image fusion evaluation

The correct fusion of multi-modal images (pre-operative and inter-operative CT, intra-operative US) is crucial in evaluating the overall performance of the entire system. Fusion errors affect the navigation errors and consequently may result in missing the target or injure the neighbor structures. Bearing this in mind, in order to ensure the patient safety and minimize the influence of possible system malfunctions, a very detailed initial verification of the image fusion has been performed on a model. Then, the final system will be verified in a clinical setting. In this study the system is verified on a specially designed phantom (shown in Fig. 8). Thus, part of the system including the analysis of pre-operative images and tracking of respiratory movements was tested in a clinical setting. However, calibration and fusion, due to the need for very precise position configuration, were tested on calibration phantom. It enables a reliable assessment of the entire system and its function as well as cooperation with the percutaneous ablation tools.

The evaluation of the personalized anatomy patient model was based on the mean DICE coefficient found for the set of segmented organs (Table 1), in relation to the outlines given by a radiologist. Clearly visible organs, not overlapped by the neighboring structures, including the liver, kidney, and ventral segment of the aorta are segmented at the level over 90% (with the liver vessels at 87%).

The calibration stage includes the spatio-temporal calibration of the ultrasound probe and the ablation needle. With the consent

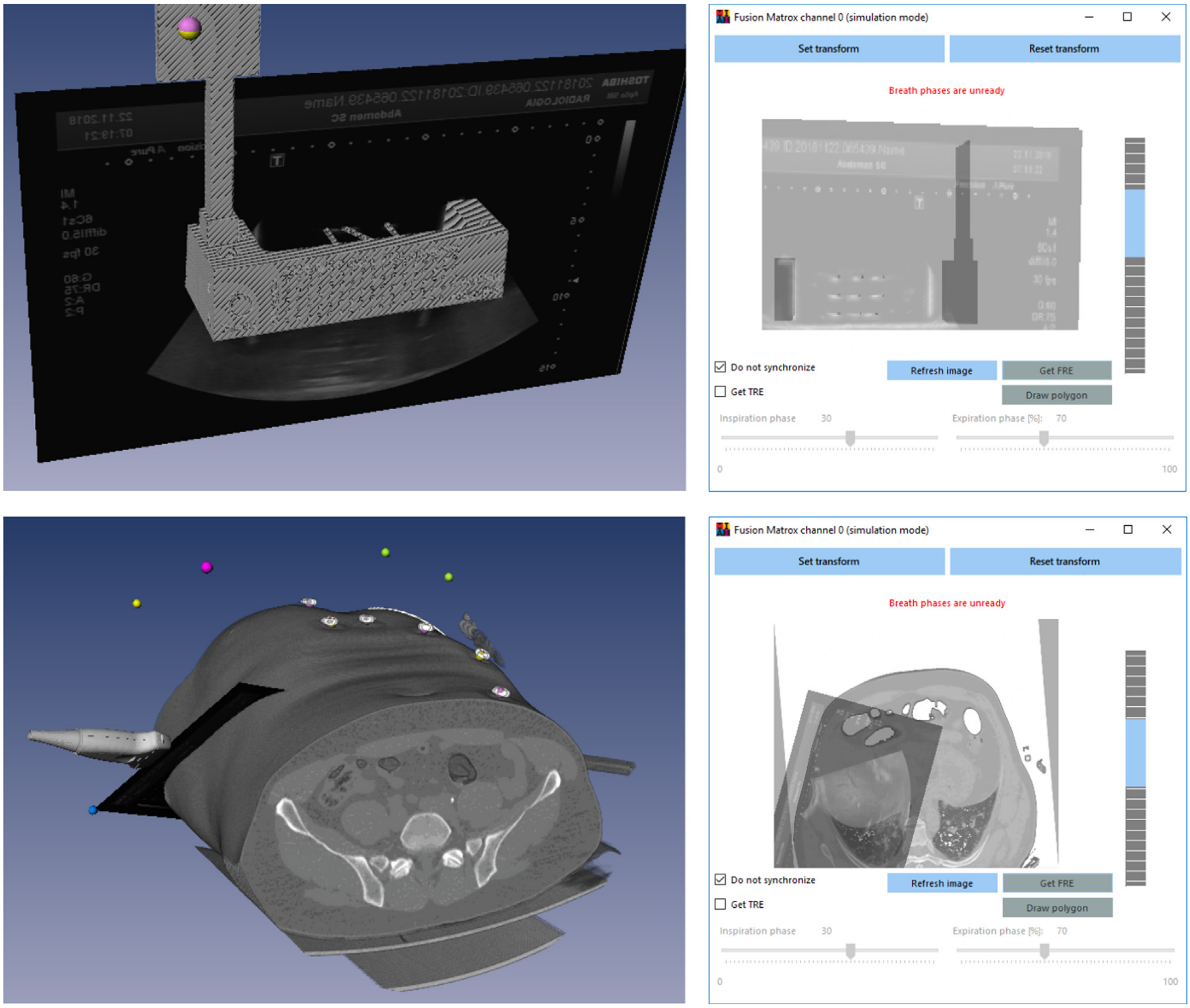

Fig. 8. US-CT fusion of calibration phantom (top): 3D scene (left), fusion window (right). Liver ablation procedure (bottom): 3D scene (left), fusion window (right).

Table 1
DICE coefficients for selected structures.

Anatomical organ	Average
Abdominal cavity	88,98 ± 2,49
Spleen	93,30 ± 3,77
Liver	90,29 ± 4,38
Right kidney	94,04 ± 0,93
Left kidney	93,43 ± 1,04
the ventral segment of the aorta	90,44 ± 2,12
Liver vessels	88,09 ± 4,70
Focal nodule	84,29 ± 3,72

Table 2
Average results obtained in an individual calibration steps.

Stylus calibration	Phantom calibration	Temporal calibration	Spatial calibration
0,51 mm	2,6 mm	006 s	1,68 mm

Table 3
Average point-based patient position registration error.

Breathing phase	Average marker fusion error
Inhale	2,03 ± 012 mm
Exhale	2,02 ± 011 mm

of the ethics committee, pilot studies in clinical settings began. The final effect of this stage in relation to the ultrasound probe is spatial calibration where an average error of 1.7 mm was obtained (Table 2). The calibration of the probe is performed before the beginning of the ablation, and the calibration of the ablation needle is performed in sterile conditions during the procedure. The developed calibration method was successfully tested in clinical conditions, where the obtained error level was clinically acceptable.

The next evaluated element of the system was the process of real time registration of a pre-operative anatomy model and patient position. Employing the developed markers placed on the abdominal surface of the patient, the average error of matching the position of the markers is about 2 mm during the entire breathing cycle (Table 3). The developed marker and the process meets the sterility requirements and was tested during clinical procedures obtaining the clinical approval.

Finally, the stage of merging the preoperative patient anatomy model with intraoperative ultrasound images was evaluated. The calibration steps described above, including the geometric calibration of system components, and the process of registering the patient position at certain breathing phases, allow the spatial and temporal CT and US image fusion to be obtained. It allows for a faster reading of intraoperative ultrasound image, which significantly facilitates the operator orientation during the procedure.

Table 4
Average point-based fusion error [mm].

Average marker fusion error
495 ± 218 mm

This stage was evaluated in clinical conditions based on images of calibration phantoms of known geometry, which allowed for a spatial evaluation of the developed method of computer aided ablation of liver tumors using the percutaneous method. The average error of fusion between the phantom points arranged in 3D reached 5 mm (Table 4).

4. Discussion

The segmentation results were compared to other multi-organ studies. Okada et al. proposed a method for finding and representing the interrelations based on canonical correlation analysis (Okada et al., 2019). The Jaccard index values for liver, spleen, right kidney, left kidney, aorta reached 90%, 85%, 81%, 82% and 78%, respectively. Another more sophisticated approach by Schreibmann et al. (2014) used a 3 stage method implementing a multi-atlas segmentation with level set-based local search. A Dice index of 91%, 86%, 88%, and 97% was reached for liver, spleen, kidneys, and aorta, respectively. Level set approach adjusted by granular computing used by Badura and Wieclawek (2016) yielded Dice index at 93%, 91%, and 94% for liver, spleen, and kidneys, respectively. Recently, Gibson et al. (2018) employed Dense V-Networks to extract abdominal organs and obtained Dice index values at 96%, 96%, 95% for liver, spleen, and left kidney, respectively. Wang et al. (2019) designed a system with organ-attention segmentation networks and local structural similarity statistical fusion for multiple abdominal structures yielding Dice index values of 98%, 97%, 98%, 97%, 92% for liver, spleen, right kidney, left kidney, and aorta, respectively. New approaches involving deep networks are able to yield higher segmentation accuracy in individual organs, yet our method is comparable in the reported structures. Moreover, none of the papers addressed the liver vasculature nor liver lesions extraction. The current study focuses more on other clinical issues important during the surgical procedure. The developed approach reduces the time required to puncture the nodule by potentially reducing the time to locate the lesion. Additional time is needed for system configuration. The average processing time for segmentation the whole patient anatomy is below 10 min. Pre surgical hardware setup and image analysis takes another 10 min. The implementation of the series of images acquired with the proposed protocol reduces the need to perform a study without contrast during the procedure, which currently was necessary to support the process of targeting the needle.

Already developed systems show the fusion of intraoperative Contrast Enhanced Ultrasound (CEUS) images with pre-operative CT images (Mauri et al., 2015) (Lee and Lee, 2018) based on a single static CT series. They also require advanced ultrasound devices with CEUS, which are not available in many facilities and are strongly operator-dependent. Earlier evaluated methods of compensation of respiratory movements were based on laparoscopic measurement of respiratory movements (Spinczyk et al., 2012, 2013a, 2013b), surface markers (Spinczyk et al., 2014; Spinczyk and Bas, 2019) or on 3DCT images (Spinczyk and Pietka, 2007; Spinczyk et al., 2013b; Fabian and Spinczyk, 2016; Spinczyk and Fabian, 2017). The proposed method combines the advantages of fusion with the methods used in radiotherapy, where the 4D series is used as a standard. It consists of 10 respiratory-gated 3D series, linearly distributed over the breath cycle. Here, the respiratory series was limited to the extreme positions of the inhalation and exhalation. This allows the amplitude of the tumor respiratory movement to be determined.

Additionally, the developed method ensures the synchronization of CT and US acquisition with the patient breathing phase of the images. This makes it easier to carry out intervention for difficult-to-reach nodules and when necessary to take into account the respiratory movements. It is even more important when multiple needle punctures are required. There are, however, high-frequency ventilation methods (Denys et al., 2014), that reduce respiratory amplitude. Yet, they increase the risk of baro-traumatic pneumothorax (Puijk et al., 2018).

The approach was tested in the 2nd Department of Radiology at the Medical University of Warsaw, Poland, during the diagnostic and planning stage of percutaneous solid ablation surgery in patients with a liver tumor.

5. Conclusions

In this study a multi-stage approach has been developed. It includes CT image acquisition protocol with the amplitude of respiratory motion that yields images subjected to a semi-automatic method able to deliver personalized abdominal model. Then, US probe and ablation needle calibration, as well as patient position adjustment method during the procedure for the pre-operative anatomy model, have been combined. Finally, an advanced module for fusion of the preoperative CT with intraoperative US images was designed. These modules have been tested on a phantom and in the clinical environment. Evaluation of the CT-US image fusion phase of the described method is under way. We plan to perform a full clinical verification of the image fusion stage on a group of 30 patients, to which the Ethics Committee of the Medical University of Warsaw has already obtained the consent.

Funding

Results of the Project, System for computer aided diagnosis and minimally invasive therapy of abdominal cancer" cofinanced by the European Union, European Regional Development Fund. Institution granting funds: The National Centre for Research and Development – ncbr.gov.pl.

References

Badura, P., Wieclawek, W., Pycinski, B., 2016. Automatic 3D Segmentation of Renal Cysts in CT. Springer, Cham, pp. 149–163, http://dx.doi.org/10.1007/978-3-319-39796-2_13.

Badura, P., Wieclawek, W., 2016. Calibrating level set approach by granular computing in computed tomography abdominal organs segmentation. Appl. Soft Comput. 49, 887–900, http://dx.doi.org/10.1016/j.asoc.2016.09.028.

Canny, J., 1986. A computational approach to edge detection. IEEE Trans. Pattern Anal. Mach. Intell. PAMI-8, 679–698, http://dx.doi.org/10.1109/TPAMI.1986.4767851.

Chan, T.F., Vese, L.A., 2001. Active contours without edges. IEEE Trans. Image Process. 10, 266–277, http://dx.doi.org/10.1109/83.902291.

Xu, Chenyang, Prince, J.L., n.d. 2019. Gradient vector flow: a new external force for snakes. Proceedings of IEEE Computer Society Conference on Computer Vision and Pattern Recognition, 66–71, http://dx.doi.org/10.1109/CVPR.1997.609299.

Cohen, L.D., Cohen, I., 1993. Finite-element methods for active contour models and balloons for 2-D and 3-D images. IEEE Trans. Pattern Anal. Mach. Intell. 15, 1131–1147, http://dx.doi.org/10.1109/34.244675.

Crocetti, L., de Baere, T., Lencioni, R., 2010. Quality improvement guidelines for radiofrequency ablation of liver tumours. Cardiovasc. Intervent. Radiol. 33, 11–17, http://dx.doi.org/10.1007/s00270-009-9736-y.

Denys, A., Lachenal, Y., Duran, R., Chollet-Rivier, M., Bize, P., 2014. Use of high-frequency jet ventilation for percutaneous tumor ablation. Cardiovasc. Intervent. Radiol. 37, 140–146, http://dx.doi.org/10.1007/s00270-013-0620-4.

Fabian, S., Spinczyk, D., 2016. Target registration error minimization for minimally invasive interventions involving deformable organs. Comput. Med. Imaging Graph., http://dx.doi.org/10.1016/j.compmedimag.2017.01.008.

Frangi, A.F., Niessen, W.J., Vincken, K.L., Viergever, M.A., 1998. Multiscale Vessel Enhancement Filtering. Springer, Berlin, Heidelberg, pp. 130–137, http://dx.doi.org/10.1007/BFb0056195.

Gibson, E., Giganti, F., Hu, Y., Bonmat, E., Bandula, S., Gurusamy, K., Davidson, B., Pereira, S.P., Clarkson, M.J., Barratt, D.C., 2018. Automatic multi-organ

segmentation on abdominal CT with dense V-Networks. IEEE Trans. Med. Imag. 37 (8), 1822–1834, http://dx.doi.org/10.1109/TMI.2018.2806309.
Gonzalez, R.C., Woods, R.E., Richard, E., Eddins, S.L., 2004. Digital Image Processing Using MATLAB. Dorsing Kindersley.
Horn, B.K.P., Hilden, H.M., Negahdaripourt, S., 1988. Closed-form solution of absolute orientation using orthonormal matrices. J. Opt. Soc. Am. A.
Juszczyk, J., Pietka, E., Pyciński, B., 2015. Granular computing in model based abdominal organs detection. Comput. Med. Imaging Graph. 46, 121–130, http://dx.doi.org/10.1016/j.compmedimag.2015.03.002.
Kass, M., Witkin, A., Terzopoulos, D., 1988. Snakes: active contour models. Int. J. Comput. Vis. 1, 321–331, http://dx.doi.org/10.1007/BF00133570.
Kenngott, H.G., Wagner, M., Gondan, M., Nickel, F., Nolden, M., Fetzer, A., Weitz, J., Fischer, L., Speidel, S., Meinzer, H.-P., Böckler, D., Büchler, M.W., Müller-Stich, B.P., 2014. Real-time image guidance in laparoscopic liver surgery: first clinical experience with a guidance system based on intraoperative CT imaging. Surg. Endosc. 28, 933–940, http://dx.doi.org/10.1007/s00464-013-3249-0.
Lasso, A., Heffter, T., Rankin, A., Pinter, C., Ungi, T., Fichtinger, G., 2014. PLUS: open-source toolkit for ultrasound-guided intervention systems. IEEE Trans. Biomed. Eng. 61, 2527–2537, http://dx.doi.org/10.1109/TBME.2014.2322864.
McClelland, J.R., Blackall, J.M., Tarte, S., Chandler, A.C., Hughes, S., Ahmad, S., Landau, D.B., Hawkes, D.J., 2006. A continuous 4D motion model from multiple respiratory cycles for use in lung radiotherapy. Med. Phys. 33, 3348–3358, http://dx.doi.org/10.1118/1.2222079.
Okada, T., Linguraru, M.G., Hori, M., Suzuki, Y., Summers, R.M., Tomiyama, N., Sato, Y., n.d., Multi-Organ Segmentation in Abdominal CT Images *. https://doi.org/10.1109/EMBC.2012.6346840.
Pereira, P.L., 2007. Actual role of radiofrequency ablation of liver metastases. Eur. Radiol. 17, 2062–2070, http://dx.doi.org/10.1007/s00330-007-0587-0.
Perona, P., Malik, J., 1990. Scale-space and edge detection using anisotropic diffusion. IEEE Trans. Pattern Anal. Mach. Intell. 12, 629–639, http://dx.doi.org/10.1109/34.56205.
Peters, T., Cleary, K. (Eds.), 2008. Image-Guided Interventions. Springer, US, Boston, MA, http://dx.doi.org/10.1007/978-0-387-73858-1.
Puijk, R.S., Ruarus, A.H., Scheffer, H.J., Vroomen, G.P.H., Van Tilborg, A.A.J.M., De Vries, J.J.J., Berger, F.H., Van Den Tol, P.M.P., Meijerink, M.R., 2018. Vascular and interventional radiology / radiologie vasculaire et radiologie d'intervention percutaneous liver tumour ablation: image guidance, endpoint assessment, and quality control. Can. Assoc. Radiol. J. 69, 51–62, http://dx.doi.org/10.1016/j.carj.2017.11.001.
Rijkhorst, E.-J., Heanes, D., Odille, F., Hawkes, D., Barratt, D., 2010. Simulating Dynamic Ultrasound Using MR-derived Motion Models to Assess Respiratory Synchronisation for Image-Guided Liver Interventions. Springer, Berlin, Heidelberg, pp. 113–123, http://dx.doi.org/10.1007/978-3-642-13711-2_11.
Schreibmann, E., Marcus, D.M., Fox, T., 2014. Multiatlas segmentation of thoracic and abdominal anatomy with level set-based local search. J. Appl. Clin. Med. Phys. 15, 4468, http://dx.doi.org/10.1120/jacmp.v15i4.4468.
Spinczyk, D., 2015. Towards the clinical integration of an image-guided navigation system for percutaneous liver tumor ablation using freehand 2D ultrasound images. Comput. Aided Surg. 20, http://dx.doi.org/10.3109/10929088.2015.1076043.
Spinczyk, D., Bas, M., 2019. Anisotropic non-rigid Iterative Closest Point Algorithm for respiratory motion abdominal surface matching. Biomed. Eng. Online 18, 25, http://dx.doi.org/10.1186/s12938-019-0643-4.
Spinczyk, D., Fabian, S., 2017. Target Registration Error minimization involving deformable organs using elastic body splines and Particle Swarm Optimization approach. Surg. Oncol. 26, http://dx.doi.org/10.1016/j.suronc.2017.09.005.
Spinczyk, D., Karwan, A., Copik, M., 2014. Methods for abdominal respiratory motion tracking. Comput. Aided Surg. 19, http://dx.doi.org/10.3109/10929088.2014.891657.
Spinczyk, D., Karwan, A., Rudnicki, J., Wróblewski, T., 2012. Stereoscopic Liver Surface Reconstruction. Wideochirurgia I Inne Tech, Maloinwazyjne, http://dx.doi.org/10.5114/wiitm.2011.28872, 7.
Spinczyk, D., Karwan, A., Zylkowski, J., Wróblewski, T., 2013a. In Vitro Evaluation of Stereoscopic Liver Surface Reconstruction. Wideochirurgia I Inne Tech, Maloinwazyjne, pp. 8, http://dx.doi.org/10.5114/wiitm.2011.32809.
Spinczyk, D., Pietka, E., 2007. Automatic Generation of 3D Lung Model. Springer, Berlin, Heidelberg, pp. 671–678, http://dx.doi.org/10.1007/978-3-540-75175-5_84.
Spinczyk, D., Zykłowski, J., Wroblewski, T., 2013b. Continuous Registration Based on Computed Tomography for Breathing Motion Compensation. Wideochirurgia I Inne Tech, Maloinwazyjne, pp. 8, http://dx.doi.org/10.5114/wiitm.2013.39505.
von Siebenthal, M., Székely, G., Lomax, A.J., Cattin, P.C., 2007. Systematic errors in respiratory gating due to intrafraction deformations of the liver. Med. Phys. 34, 3620–3629, http://dx.doi.org/10.1118/1.2767053.
Wang, Y., Zhou, Y., Shen, W., Park, S., Fishman, E.K., Yuille, A.L., 2019. Abdominal multi-organ segmentation with organ-attention networks and statistical fusion. Med. Image Anal. 55, 88–102, http://dx.doi.org/10.1016/j.media.2019.04.005.